Catalysis Science & Technology

Accepted Manuscript

ROYAL SOCIETY OF CHEMISTRY

www.rsc.org/catalysis

Catalysis Science & Technology

ARTICLE

Crystal-plane effect of nanoscale CeO_2 on the catalytic performance of Ni/CeO_2 catalysts for methane dry reforming

Received 00th January 20xx,
Accepted 00th January 20xx

DOI: 10.1039/x0xx00000x

www.rsc.org/

Ning Wang,[a] Weizhong Qian,[*,a] Wei Chu[*,b], and Fei Wei[a]

The morphology and crystal-plane effects of CeO_2 materials (nanorods, nanocubes, nanooctas and nanoparticles) on the catalytic performance of Ni/CeO_2 in the methane dry reforming were investigated. The XRD and Raman results showed that Ni species can be incorporated into the lattices and induce the increase of oxygen vacancy by occupying the vacant sites in the CeO_2 nanomaterials. The reaction experiments showed that the catalysts supported over CeO_2 nanorods achieved significant higher catalytic activity and a better stability than the other three catalysts. This improved activity was closely related to the strong metal-support interaction between Ni and CeO_2 nanorods, which showed great superiority for anchoring Ni nanoparticles. The oxygen vacancies and the mobility of lattice oxygen also showed the morphology dependence. They can participate into the catalytic reaction and be favorable for the elimination of carbon deposition. The resistance to carbon deposition was found over the Ni/CeO_2-nanorods catalyst, whereas amounts of graphitic carbon species were formed over the Ni/CeO_2-nanocubes catalysts, which was responsible for deactivation.

Introduction

In recent years, much attention has been directed towards the control and utilization of greenhouse gases (carbon dioxide and methane).[1-3] Carbon dioxide reforming of methane (or methane dry reforming) is an efficient route for consumption of these two greenhouse gases.[4-7] It can produce synthesis gas (syngas) with low H_2/CO ratio, which is suitable for obtaining valuable hydrocarbons through Fischer-Tropsch (F-T) synthesis and oxo-synthesis.[8] Ni-based catalyst is one of the desirable catalysts due to its high catalytic activity, low cost, and extensive availability. However, the Ni-based catalyst is inclined to deactivate during the long-term stability test because of the carbon deposition and sintering of the metallic and support phases.[9-11] Thus, how to improve the resistance ability of carbon deposition and the metal sintering is still a hot topic in the methane dry reforming reaction.

Ceria is an important support material, which can enhance the catalytic property via promoting the dispersion of the active component and increasing the metal-support interaction.[6, 12] Moreover, its unique property benefits from the rapid and reversible interchange between Ce^{3+} and Ce^{4+}, making it an oxygen buffer. Thus, it can be widely used as active component or support in many catalytic reactions, such as CO oxidation, water-gas shift reactions, NO catalytic reduction, catalytic partial oxidation of methane, and methane reforming.[13-17]

In recent years, the catalytic performance of CeO_2 is found to be significantly influenced by the nature of the exposed lattice planes. In general, different CeO_2 shapes may expose different crystal planes in CeO_2 crystal structure. For example, CeO_2 nanorods (NRs) incline to preferentially expose four {110} and two {100} planes, while the CeO_2 nano-octahedrons (NOs) expose eight {111} planes.[18] The different crystal planes of ceria shows different properties such as the formation energy of oxygen vacancies,[19] the interaction with the surface molecules,[20] and the stability.[21] Mai et al reported that oxygen storage took place at the surface as well as bulk over NRs and nanocubes (NCs), whereas oxygen storage was limited to bulk in nanoparticles (NPs).[18] The density functional theory has shown that the chemical activity of different CeO_2 planes follow the order of {110} < {100} < {111}.[22-26] This implies that the formation of oxygen vacancies are easier on the CeO_2 {110} planes. On the other hand, studies have shown that the crystal facet of the CeO_2 support played an important role on the active metal. The dispersion of active metal and the incorporation of metal into the CeO_2 lattice were both thought to cause the physicochemical modifications. So far, many works about the shape effect of CeO_2 support have been reported on CO oxidation,[27] ethanol reforming,[21, 28] and water–gas shift.[29]

CeO_2 supports with different morphologies shows different oxygen mobility and intensity of interaction with active metal particles, which can affect the gasification of carbon species and thermal sintering of Ni particles. In our previous study,[6, 30-

[a] Beijing Key Laboratory of Green Chemical Reaction Engineering and Technology, Department of Chemical Engineering, Tsinghua University, Beijing, 100084, P.R. China. E-mail: qianwz@tsinghua.edu.cn
[b] Department of Chemical Engineering, Sichuan University, Chengdu 610065, P.R. China. E-mail: chuwei1965@scu.edu.cn
† Electronic Supplementary Information (ESI) available. See DOI: 10.1039/x0xx00000x

[32] the CeO_2 and Ce-containing mixed oxide ($Ce_{1-x}Zr_xO_2$, Ce-SBA-15, CeO_2-Al_2O_3, et al) have been investigated in methane dry reforming. It can be found that cerium, used as support or promoter, can improve the dispersion of Ni active species obviously and inhibit the carbon formation due to the high amount of mobile oxygen. However, until now, very little is known for Ni/CeO_2 composite nanomaterials with respect to the morphology effect of CeO_2 on the chemical state and catalytic performance of nickel species as highly active catalysts for the methane dry reforming. More detail works are required for better understanding the structure-performance relationship. Therefore, on the basis of these ideas, four different nanostructures of ceria (rod, cube, octahedron, and particle) were prepared using a facile precipitation-hydrothermal method. Ni species were deposited on CeO_2 by the impregnation method. The correlations between the catalytic stability and the oxygen mobility ability of ceria support were studied for this reaction. The interaction between nickel and different crystal orientations were elucidated. The aim was to investigate the potential shape effects of the CeO_2 nanocrystals on the methane dry reforming reaction.

Experimental Section

Synthesis Procedures

CeO_2 nanorod (NRs), nanocubes (NCs), nanooctas (NOs) and nanoparticles (NPs) were prepared by the improved hydrothermal method as reported previously.[33] To obtain nanorods and nanocubes, 1.74 g of $Ce(NO_3)_3{\cdot}6H_2O$ and the desired amount of NaOH (C_{NaOH}; see below) were first dissolved in 40 mL of deionized water, respectively. Then, these two solutions were mixed and kept stirring for 30 min with the formation of milky suspension. Subsequently, the mixed solution was transferred into a Teflon-lined stainless steel autoclave and then heated at different temperature (T) for 24 h. After the hydrothermal treatment, the precipitates were washed with distilled water and ethanol, then dried at 60 °C for 12 h and calcined at 700 °C for 4 h in air at a heating rate of 5 °C min^{-1}.

The values of C_{NaOH} and T were varied according to the target crystal shape (NRs: C_{NaOH} = 6 M, T = 100 °C; NCs: C_{NaOH} = 6 M, T = 180 °C; NOs: 0.1M, T = 180 °C; NPs: C_{NaOH} = 0.1M, T = 100°C).

The Ni/CeO_2 catalysts were prepared using the incipient impregnation method. CeO_2 powder was mixed with $Ni(NO_3)_2{\cdot}6H_2O$ solution under magnetic stirring at 80 °C to achieve 5% Ni/CeO_2. After stirring, the solution was dried and then calcined in air at 700 °C for 1 h at a heating rate of 5 °C min^{-1}.

Characterization

The X-ray diffraction patterns (XRD) were carried out on an X-ray diffraction apparatus (Philips X' pert PRO) with Cu Kα (45 kV, 50 mA) radiation. Raman spectra were recorded using excitation wavelength of 325 nm and 532 nm on a Renishaw (RM2000) spectrometer. The morphology of the materials was visualized using a JEOL JEM 2010 transmission electron micro-scope (TEM) operated at 120.0 kV. The samples were dispersed in ethanol assisted by ultrasonic technique. The X-ray photoelectron spectra (XPS) were recorded on the XSAM800 spectrometer with an Al Kα (hν = 1486.6 eV) X-ray source. Charging effects were corrected by adjusting the binding energy of C 1s peak from carbon contamination to 284.6 eV. Temperature-programmed reduction (TPR) experiments were carried out in a fixed-bed reactor. Prior to the TPR measurements, samples were pretreated at 300 °C for 0.5 h in flowing Ar (50 mL/min) to remove any moisture and adsorbed impurities. After cooling the reactor to the room temperature, the reduction gas of 5% H_2/N_2 with a flow rate of 30 mL/min was introduced. The temperature of the reactor was raised linearly to 800 °C at a rate of 10 °C/min by a temperature controller. The hydrogen consumption was analyzed on-line by a SC-200 gas chromatograph with a thermal conductivity detector (TCD). Hydrogen chemisorption was performed in a static volume apparatus Autosorb-1-C (Quantachrome). The samples were first dried under He atmosphere at 250 °C for 2 h and reduced in purified H_2 at 700 °C for 1 h using a heating rate of 10 °C/min. The samples were purged with helium at this temperature for 2 h, and then cooled down in vacuum to 40 °C for the chemisorption measurement. The hydrogen monolayer uptake of the catalysts was calculated by extrapolating the isotherm to zero pressure. An adsorption stoichiometry of one hydrogen adsorbed per surface Ni atom was assumed. The Ni particle size was calculated using the formula,dNi=6V/S, where V is the volume of total metallic Ni and S is the active Ni surface area assuming the Ni particles were spherical in shape. The percentage of Ni dispersion was calculated by dividing the number of exposed surface Ni atoms (determined by H_2 chemisorption) by the total number of Ni atoms in the catalyst. The amount of carbon deposited on the used samples was determined with a thermo gravimetric analyzer (TGA Q500). The sample was heated in flowing air from room temperature to 800 °C at a heating rate of 10 °C/min. Chemical analysis of the samples was carried out by means of the ICP (Inductively Coupled Plasma) spectroscopy with TJA IRIS 1000 Radial ICP-AES equipment. The error of analysis for each element was Ni±0.70%, Ce±0.08%. The oxygen storage capacity (OSC) was measured at 700 °C under atmospheric pressure in a fixed bed flow microreactor. Then 100 mg of CeO_2 was diluted with 400 mg of quartz sand (40–60 mesh) and placed in a U-shaped quartz tube. After the sample was oxidized at 700 °C in O_2 (5%)/He flow for 15 min, and flushed with pure He to remove O_2 contamination, H_2 (5.0% in He) was pulsed into the reactor and the sample was fully reduced at 700 °C by several times pulses at intervals of 1 min. Afterward, O_2 (5% in He) pulses were introduced at the same temperature to complete the reduction–oxidation cycle of the samples. The H_2–OSC values were determined by the amount of H_2 consumed during the H_2 pulses analyzed by on-line gas chromatography using a thermal conductivity detector. Each measurement was repeated four times and the results were averaged.

Catalytic performance testing

The catalytic activity measurements were carried out under atmospheric pressure using a continuous fixed-bed flow reactor. Typically, 100 mg of catalyst was loaded in the reactor using quartz wool. The molar ratio of CH_4 to CO_2 was 1:1 and GHSV was 36,000 mL/(h·g_{cat}). The catalyst was reduced in the reactor with H_2 at 700 °C for 1 h before test. Effluent gases from the reactor were analyzed on-line by a GC-1690 model gas chromatograph with a TDX-01 column and a thermal conductivity detector (TCD). The conversions of CH_4 (X_{CH4}) and CO_2 (X_{CO2}), the selectivities of CO (S_{CO}) and H_2 (S_{H2}), and syngas ratios were calculated by using Eqs. (1)–(5):

$$X_{CH_4} = \frac{(F_{CH_4,in} - F_{CH_4,out})}{F_{CH_4,in}} \times 100\% \quad (1)$$

$$X_{CO_2} = \frac{F_{CO_2,in} - F_{CO_2,out}}{F_{CO_2,in}} \times 100\% \quad (2)$$

$$S_{CO} = \frac{F_{CO,out}}{(F_{CH_4,in} + F_{CO_2,in}) - (F_{CH_4,out} + F_{CO_2,out})} \times 100\% \quad (3)$$

$$S_{H_2} = \frac{F_{H_2,out}}{2(F_{CH_4,in} - F_{CH_4,out})} \times 100\% \quad (4)$$

$$Ratio\ of\ H_2/CO = \frac{F_{H_2,out}}{F_{CO,out}} \quad (5)$$

where $F_{i,\ in/out}$ was the flow rate of each component in the feed or effluent.

Results and discussions

Catalyst characterization

The TEM images of ceria nanomaterials were shown in Fig. 1. The CeO_2-NRs displayed a uniform diameter of 11.5±1.0 nm and a less-uniform length in the range 99.4±6.3 nm (Fig. 1a). Combining the HRTEM images (Fig. 1b) with the selected area electron diffraction (SAED) analysis (inset), two kinds of lattice fringe directions attributed to (200) and (220) planes were observed for the CeO_2-NRs, which had an inter-plane spacing of 0.27 and 0.19 nm, respectively. Hence, the CeO_2-NRs grew along the [110] direction and predominantly exposed the less stable {110} (located as two side facets and two cross section facets) and {100} (located as two side facets) planes.[25, 34] According to the average size of CeO_2-NRs and the locations of {110} and {100} planes, the fractions of {110} planes and {100} planes were ca. 51% and ca. 49%, respectively. The CeO_2-NCs showed a smooth surface and uniform size distribution in 18.8±1.3 nm (Fig. 1c). All of the CeO_2-NCs were observed in perfect cubic shape. The HRTEM images and SAED pattern in Fig. 1d showed that the lattice fringes corresponded to the (200) and (020) plane (belonging to {100} plane) with the inter-plane spacing of 0.27 nm. The plane-intersecting angle was 90°. The morphology of most of the CeO_2-NCs was compatible with a cube enclosed by six {100} planes.[35] Fig. 1e showed the TEM images of uniform CeO_2-NOs with the size of 20.0±3.3 nm. The HRTEM images (Fig. 1f) showed the (111) lattice fringes with the inter-plane spacing of 0.32 nm and a plane-intersecting angle of 70.5°. This indicated that the CeO_2-NOs were dominated by the truncated octahedral shape enclosed by the (111) facets. Such an octa-shape was observed in previous studies.[18, 26, 36-38] The CeO_2-NPs had a size of 16.3±0.4 nm (Fig. 1g). The HRTEM images showed that the CeO_2-NPs exposed mainly {111} planes together with {100} planes (Fig. 1h).

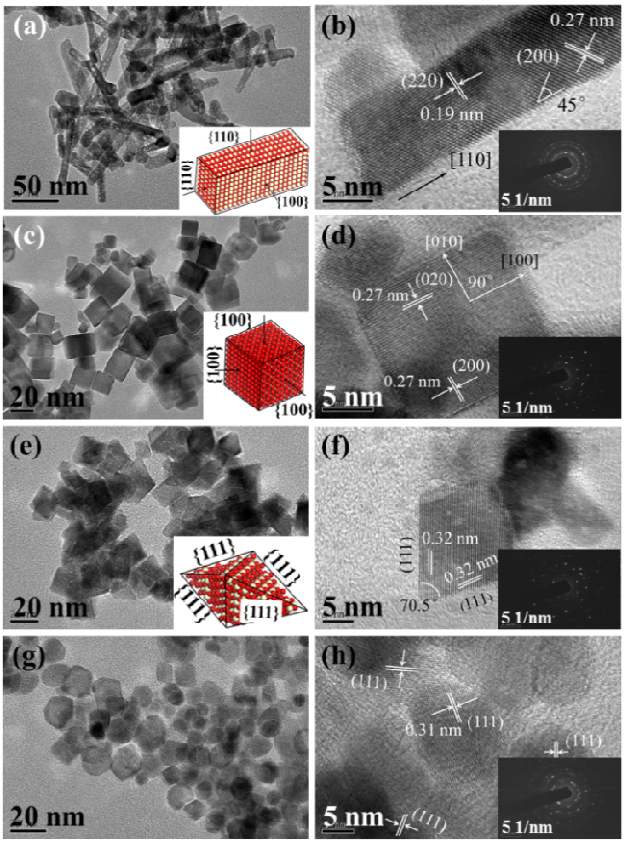

Fig. 1 TEM, HRTEM and SAED (inset) images of as-obtained CeO_2: (a, b) NRs, (c, d) NCs, (e, f) NOs, and (g, h) NPs.

The XRD patterns for the various ceria nanomaterials (shown

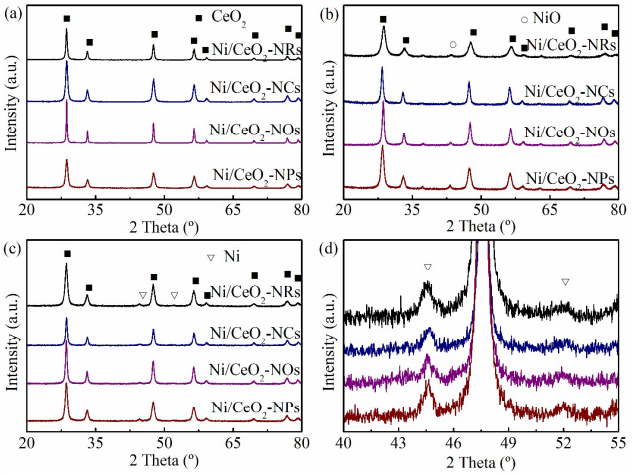

Fig. 2 XRD patterns of (a) CeO_2, (b) caicined Ni/CeO_2, and (c) (d) reduced Ni/CeO_2.

Table 1 The BET surface areas (S_{BET}), lattice parameter (a_0), crystalline size, and the microstrain (ε) of ceria in Ni/CeO_2 samples.

Samples	S_{BET} (m^2/g)	$d_{(111)}$-spacing (nm)	Lattice parameter (nm)	Crystalline size (nm)	ε (%)
Ni/CeO_2-NRs	76.4	0.3103	0.5374	14.8	0.6346
Ni/CeO_2-NCs	12.6	0.3109	0.5385	21.9	0.4007
Ni/CeO_2-NOs	74.6	0.3109	0.5385	23.8	0.4171
Ni/CeO_2-NPs	52.7	0.3107	0.5381	21.8	0.3484

in Fig. 2a) were characteristic of the face-centered cubic fluorite structure of ceria (PDF 65-5923, space group Fm3m). The wider diffraction peaks of the CeO_2-NRs implied a smaller crystallite size compared to the other three CeO_2 nanomaterials. After introducing nickel, the ceria remained in the original face-centered cubic structure with the appearance of weak NiO diffraction peak at 37.0° and 43.0° (Fig. 2b). However, the lattice parameters (a_0) of ceria decreased (Table 1) with a slight shift in position of diffraction peaks. The lattice contraction was related to the incorporation of nickel with the smaller ion radius (r_{Ni}^{2+} = 0.72 Å) into the lattice of ceria (r_{Ce}^{4+} = 0.94 Å).[39] In addition, compared to that of pure ceria nanomaterials, the crystallite size of ceria over Ni/CeO_2 increased, which was probably associated with the slight sintering during the process of thermal calcination. As shown in Table 1 and Table S1, the CeO_2-NRs showed the highest microstrain both before and after loading nickel, and the CeO_2-NPs had the least strain. According to the previous report,[40] the strain was a measurement of lattice stress existing in the materials because of lattice distortion, elongation or contraction. Thus, the variation of strain implied that the concentration of oxygen vacancies in CeO_2-NRs was larger than the other three ceria materials.

The oxygen storage capacity (OSC) of ceria was investigated by O_2–H_2 titration methods for four consecutive cycles. From Fig. S1, It can be observed that the OSC of the samples at 700°C showed significant differences. The CeO_2-NRs exhibited an OSC of 587 μmol H_2/g, which was much higher than that of CeO_2-NCs and CeO_2-NOs (the value was about 314 and 347 μmol H_2/g, respectively), due to easier formation of oxygen vacancies on (110) than on (100) and (111). In addition, after four consecutive cycles, H_2 consumption of the CeO_2-NRs maintained stable, but the OSC of CeO_2-NCs and CeO_2-NOs decreased continuously with the O_2–H_2 titration. This suggested that the CeO_2-NRs were of more reversible redox behavior.

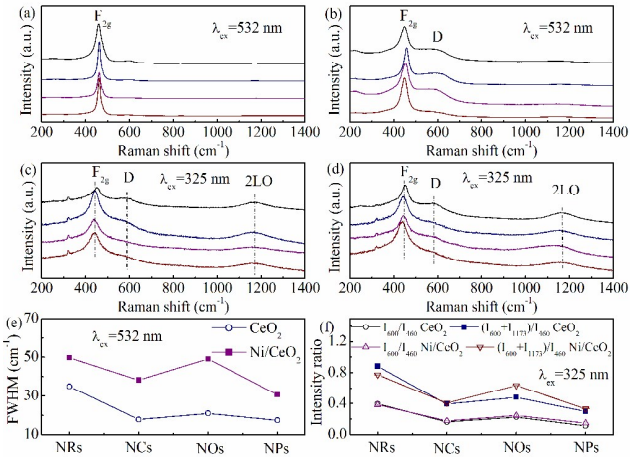

Fig. 3 Visble Raman spectra of (a) CeO_2 and (b) Ni/CeO_2. UV Raman spectra of (c) CeO_2 and (d) Ni/CeO_2. (e) FWHM of F_{2g} peak and (f) the corresponding peak intensity ratios I_{600}/I_{460}, $(I_{600}+I_{1173})/I_{460}$.

The H_2-TPR profiles showed that four ceria samples exhibited a single reduction peak at 350–600°C (Fig. S2), and the peak temperature of CeO_2-NRs was the lowest, followed by CeO_2-NCs and CeO_2-NOs, was about 480, 505 and 510°C, respectively. However, the H_2-consumption (peak area) increased with CeO_2-NCs, CeO_2-NOs and nanorod. Simultaneously, the multiple H_2-TPR profiles showed that the CeO_2-NRs were of higher stability.

After reduction in hydrogen atmosphere at 700 °C for 1 h, the formation of metallic Ni were observed through diffraction lines at 2θ values of 44.5° and 51.8° (Figs. 2c and d). These two diffraction peaks were associated with (111) and (200) planes of Ni in the structure. The Ni diffraction peaks were very weakly resolved for all the Ni/CeO_2 samples, suggesting good dispersions of Ni particles. The calculation of Ni crystalline size was not attempted because of low intensity of Ni diffraction peaks. The BET specific surface areas of CeO_2-NRs, CeO_2-NOs and CeO_2-NPs were measured to be 80.5, 80.2 and 82.8 $m^2 \cdot g^{-1}$, which were more than three times than that of CeO_2-NCs (Table S1).

The XRD results can be complemented by the Raman spectra, which detected the structural changes of ceria lattice caused by the shapes and introducing nickel. Figs. 3a and b presented the visible (532 nm) Raman spectra of ceria supports and Ni/CeO_2 catalysts, respectively. A strong vibration mode (F_{2g}) of ceria phase at about 462 cm^{-1} can be observed in Fig. 3a, which can be attributed to the symmetrical stretching vibration of the oxygen atoms around cerium ions.[41] The full width at half maximum (FWHM) values of F_{2g} peaks increased in the order: CeO_2-NPs < CeO_2-NCs < CeO_2-NOs < CeO_2-NRs (Fig. 3e). The band broadening of F_{2g} line was associated to high concentration of oxygen defects.[42] The Raman spectra of Ni/CeO_2 were similar to those of supports (Fig. 3b). The bands of nickel species were not detected, indicating their dispersion state. The incorporated nickel species resulted in not only the increase of FWHM values, but also to the slight red shift of F_{2g}

peaks. This red shift to 448 cm^{-1} together with band broadening suggested that the deposition of Ni composition lowered the symmetry of Ce-O bond and resulted in an increased optical absorption (yellow on CeO_2 while black on Ni/CeO_2).[43]

As the UV Raman spectra were more sensitive to defect sites in ceria than the visible Raman,[44] the UV Raman measurement under an excitation wavelength of 325 nm were performed (Figs. 3c and d). The Raman shifts at 450 cm^{-1}, 567 cm^{-1} and 1173 cm^{-1}, were ascribed to the F_{2g} symmetry mode, defect-induced mode (D bond), and seconded-order longitudinal optical mode (2LO bond), respectively.[45] The D bond at around 567 cm^{-1} was related to the presence of oxygen vacancies due to the presence of Ce^{3+} ions in ceria lattice, and the relative intensity ratio of I_D/IF_{2g} reflected the concentration of oxygen vacancy in ceria.[49] Introducing nickel led to a lower intensity of F_{2g} band while a higher intensity of D band. In addition, the peak at 567 cm^{-1} for defects presented a blue shift to 579 cm^{-1}, and the peaks at 1173 cm^{-1} were widened obviously. These changes (the shifts and broadening) can be due to the fact that some nickel inserted into the lattice of ceria and formed $Ce_{1-x}Ni_xO_2$ solid solution.[46]

Moreover, in the cases of CeO_2 and Ni/CeO_2 with various morphologies, the I_{600}/I_{460} and $(I_{600}+I_{1173})/I_{460}$ values decreased in the following the sequence: CeO_2-NRs > CeO_2-NOs > CeO_2-NCs > CeO_2-NPs, as displayed in Fig. 3f. This indicated that the amount of the oxygen vacancies of as-obtained ceria varied as nanorod > nanoocta > nanocube > nanoparticle. After loading the nickel oxide, all of the intensity ratios increased clearly. This finding implied that the nickel species were incorporated into the lattice of CeO_2 and induced the increase of oxygen vacancy. Moreover, Ni/CeO_2-NRs showed the highest value among them, which further reveal that the interaction between nickel and ceria rod was stronger than that with the other ceria materials. Therefore, the morphology of ceria nanomaterials had a significant impact on the synergistic interaction between nickel and ceria.

XPS spectra were used to investigate the surface composition and chemical states of cerium and nickel. The complex spectrum of Ce3d was numerically fitted with eight components with the assignments defined in Fig. 4a. The bands labeled u and v, u_2 and v_2, u_3 and v_3 were characteristic of Ce^{4+}, while the other two bands labeled v_1 and u_1 represented $3d^{10}4f^1$ initial electronic state corresponding to Ce^{3+}.[47] Therefore, the chemical valence of cerium on the surface of these reduced samples was mainly in a +4 oxidation state, and a small amount of Ce^{3+} co-existed. There was an increase in the binding energy value of the $Ce3d_{5/2}$ component (883.7 eV) compared to that of pure CeO_2 (882.9 eV).[48] This shift can be explained by the interaction between nickel and cerium oxide, namely, the incorporation of Ni into the surface lattice of cerium. Moreover, the content of Ce^{3+} can be calculated from the area of u_1 and v_1, according to the following formula: [49]

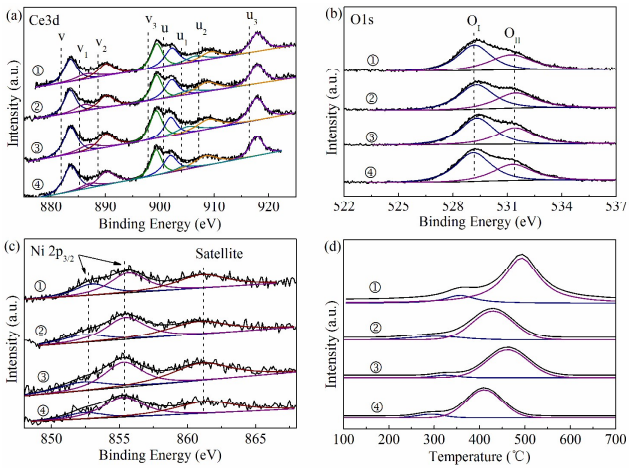

Fig. 4 XPS spectra of (a) Ce3d, (b) Ni2p, and (c) O1s for reduced Ni/CeO_2. (d) H_2-TPR profiles of Ni/CeO_2: ① Ni/CeO_2-NRs, ② Ni/CeO_2-NCs, ③ Ni/CeO_2-NOs, ④ Ni/CeO_2-NPs.

$$Ce^{3+}(\%) = \frac{S_{u1} + S_{v1}}{\sum (S_u + S_v)} \times 100$$

Table 2 presented the relative contributions of Ce^{3+} and Ce^{4+} that calculated through peak fitting and using the areas under the fitted components. The $Ce^{3+}/(Ce^{4+}+Ce^{3+})$ ratio was observed to be dependent of the morphology. It can be seen that the Ce^{3+} contents in Ni/CeO_2 decreased in the sequence: Ni/CeO_2-NRs > Ni/CeO_2-NOs > Ni/CeO_2-NCs > Ni/CeO_2-NPs. In the previous literatures, it has been reported that the presence of oxygen vacancy can promote the transformation of Ce^{4+} to Ce^{3+}.[21, 50] Thus, combined with the Raman results, this phenomenon can be explained by the formation of more surface oxygen vacancies over Ni/CeO_2-NRs.

The spectrum of O1s was fitted with two Gaussian peaks, as displayed in Fig. 4b. The main peak at ~529.3 eV was attributed to the lattice oxygen bonding to the metal cations, and an additional peak at ~531.4 eV to the chemisorbed oxygen (surface adsorbed water and C-O species).[48] The adsorption of CO and CO_2 in the reduced state Ce^{3+} sites has a higher thermal stability than those in the Ce^{4+} sites.[51, 52] Thus, the adsorbed oxygen was derived from carbonate species trapped by oxygen vacancies. The content of oxygen vacancies can be obtained from XPS relative percentage of adsorbed oxygen. The XPS results of the lattice oxygen (O_I) and the adsorbed oxygen (O_{II}) were shown in Table 2. The proportion of $O_{II}/(O_I+O_{II})$ of these samples presented a sequence: Ni/CeO_2-NRs > Ni/CeO_2-NOs > Ni/CeO_2-NCs > Ni/CeO_2-NPs, which was in agreement with the order of Ce^{3+} content. The high concentration of oxygen species on Ni/CeO_2-NRs was due to its (110) plane with high chemical activity, which were active sites for the chemisorption of oxygen from CO_2 and H_2O. The oxygen vacancies acted as the act site for activating CO_2 and the activated CO_2 can react with the deposited carbon.

Fig. 4c showed the Ni2p$_{3/2}$ XPS spectra of reduced Ni/CeO$_2$ catalysts. The peak at ~852.3 eV and ~855.4 eV were characteristic of Ni and NiO, respectively. The relative contributions of the two species was calculated from the areas under the fitted components and displayed in Table 2. It can be observed that more Ni^{2+} was reduced to Ni^0 over the Ni/CeO$_2$-NRs compared with that over the other three catalysts, indicating that the Ni/CeO$_2$-NRs had a higher reducibility of Ni species. In addition, the Ni/CeO$_2$-NRs showed the lowest Ni/Ce molar ratio, while the Ni/CeO$_2$-NPs showed the highest one. Moreover, the surface Ni/Ce ratios of Ni/CeO$_2$-NCs and Ni/CeO$_2$-NPs were obviously higher than the counterpart bulk values, respectively. Combined with the Raman spectra and TEM results, the low Ni/Ce ratio of Ni/CeO$_2$-NRs was ascribed to the incorporation of nickel species into the first surface layer of ceria and insertion inside the pores, which can restrain the sintering of Ni particles.[53] In the case of Ni/CeO$_2$-NCs, the higher surface content of nickel can be attributed to the lower available surface area. In this case, Ni particles were partially segregated on the surface, which grew easily into larger particles.

The TPR measurements were performed in Fig. 4d, which demonstrated that the Ni-CeO$_2$ interaction followed the order: Ni/CeO$_2$-NRs > Ni/CeO$_2$-NOs > Ni/CeO$_2$-NCs > Ni/CeO$_2$-NPs. There were two reduction peaks for all of the catalysts. It was reported that the reduction of Ni^{2+} to Ni^0 did not go through intermediate oxides,[54,55] so the H_2 consumption peaks appearing in different temperature regions can be ascribed to the reduction of different species. The first reduction peak was attributed to the reduction of weakly interactive NiO species with ceria support. The second peak can be ascribed to the reduction of strongly interactive NiO species with ceria support. The second reduction peak of Ni/CeO$_2$-NRs shifted to higher reduction temperature, indicating a stronger interaction between Ni and CeO$_2$. Besides, the H_2 consumption of the second peak on the Ni/CeO$_2$-NRs was more than that on the Ni/CeO$_2$-NPs, suggesting that a larger amount of strong interactive NiO species existed on the CeO$_2$-NRs. According to the report by Shan,[56] the Ni species incorporated into CeO$_2$ lattice were difficult to reduce, so the peak that belonged to this type of Ni species did not appear in the profiles. As Ni/CeO$_2$-NCs exposed {100} planes while Ni/CeO$_2$-NRs exposed {110} and {100} planes, it was likely that the Ni particles preferentially interacted with the {110} crystal planes.

Table 2 The XPS analysis of the catalysts

Catalysts	$Ce^{3+}/(Ce^{3+}+Ce^{4+})$	$Ni^0/(Ni^0+Ni^{2+})$	$O_{II}/(O_I+O_{II})$	Ni/Ce	
				Surface [a]	Bulk [b]
Ni/CeO$_2$-NRs	0.153	0.350	0.459	0.156	0.173
Ni/CeO$_2$-NCs	0.109	0.297	0.396	0.202	0.186
Ni/CeO$_2$-NOs	0.129	0.302	0.429	0.182	0.192
Ni/CeO$_2$-NPs	0.081	0.252	0.373	0.231	0.172

[a] The surface Ni contents were determined by XPS analysis.
[b] The bulk Ni contents were determined by EDX analysis.

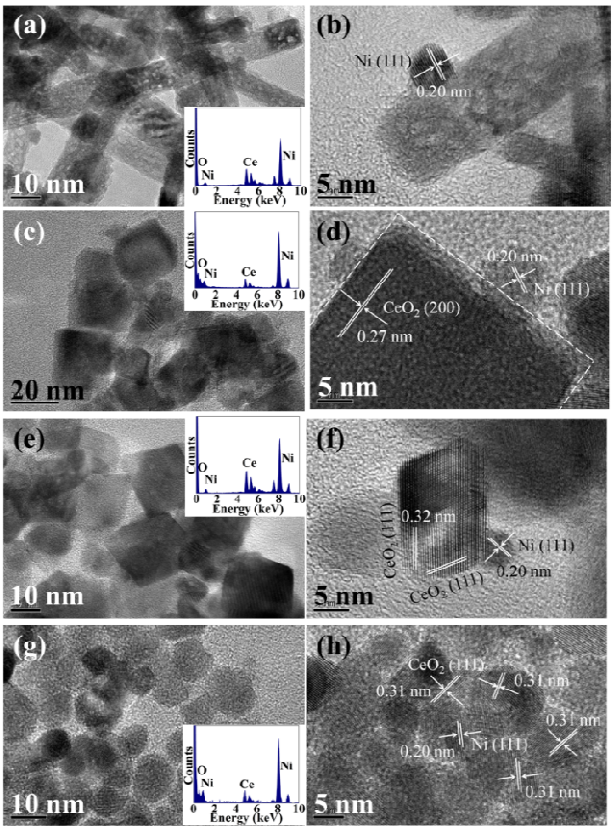

Fig. 5 TEM images and the corresponding EDX spectra of Ni/CeO$_2$: (a, b) Ni/CeO$_2$-NRs, (c, d) Ni/CeO$_2$-NCs, (e, f) Ni/CeO$_2$-NOs, and (g, h) Ni/CeO$_2$-NPs.

The actual Ni loading amount on the samples were listed in Table S2, as measured by ICP. It can be observed that the actual Ni mass percentage were between 4.4wt%-4.8wt%, close to the theoretical content (5.0wt%). Combined the ICP and TPR results, the reducibility were calculated and also summarized in Table S2. Ni/CeO$_2$-NRs sample showed the highest reducibility, while Ni/CeO$_2$-NPs had the lowest one.

The TEM images showed that the four different shaped ceria nanomaterials maintained their original crystal shapes after impregnating Ni and subsequent heat treatments (Fig. 5). The EDS spectra confirmed the existence of Ni composite. From the HRTEM images, it can be observed that the Ni NPs with exposed (111) planes were homogeneously dispersed on CeO$_2$ supports for all the samples. By counting more than 50 Ni NPs for each sample, we got the average sizes of Ni nanoparticles in Ni/CeO$_2$-NRs, Ni/CeO$_2$-NOs, Ni/CeO$_2$-NCs and Ni/CeO$_2$-NPs samples, which did not differ much and were 6.1, 5.7, 5.8 and 5.0 nm, respectively. It can be found that the difference among all the samples was no more than 1 nm, which was in line with the H_2-chemisorption results in Table 3. Almost all the counted Ni NPs in the samples are supported on the faces of CeO$_2$ nanocrystals rather than on their edges and truncated corners.

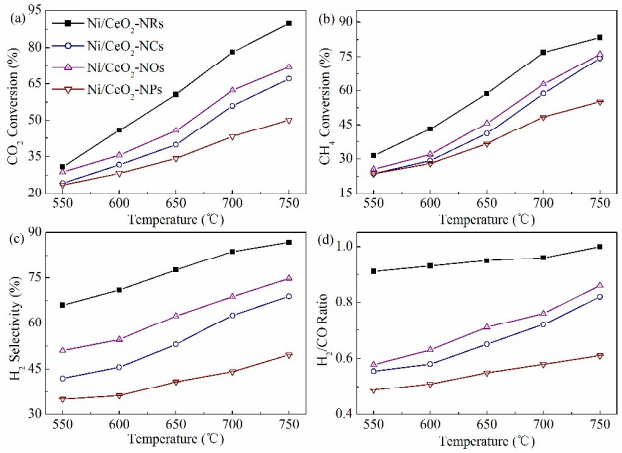

Fig. 6 The effect of temperature on the initial catalytic performance of Ni/CeO_2 samples.

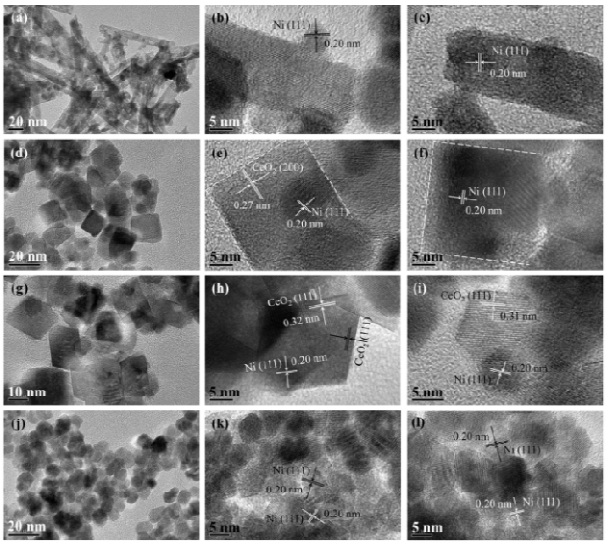

Fig. 7 TEM images for Ni/CeO_2 catalysts after catalytic activity test: (a-c) Ni/CeO_2-NRs, (d-f) Ni/CeO_2-NCs, (g-i) Ni/CeO_2-NOs, and (j-l) Ni/CeO_2-NPs.

As the CeO_2-NRs had more oxygen vacancies which were important for anchoring the Ni active particles, the SMSI effect existed between Ni and CeO_2-NRs. Some of the CeO_2-NRs can be reduced due to the hydrogen spillover and it covered the Ni NPs at the same time. However, it can appear again on the surface after the evacuation of H_2 stream.[57] Thus, the surface of CeO_2-NRs was rough.

Catalytic performances of Ni/CeO_2

Fig. 6 compared the initial catalytic activity as a function of reaction temperature over Ni/CeO_2 catalysts with different morphology. The bare CeO_2 materials did not show any catalytic activity in this reaction under the investigated experimental conditions (not shown). The initial conversions of reacting gases over the catalysts were clearly dependent on reaction temperature. The CO_2 and CH_4 conversions increased with increasing the temperature, which was characteristic of the endothermic character of methane dry reforming. The activities of four samples can be ranked: Ni/CeO_2-NRs > Ni/CeO_2-NOs > Ni/CeO_2-NCs > Ni/CeO_2-NPs. The CH_4 conversion was predominantly from its dissociation on active nickel particles at 550 °C, so the similar CH_4 conversion values can be observed at this temperature for all of the samples. With increasing the temperature, the oxygen mobility enhanced and the lattice oxygen atoms were also involved in the CH_4 conversion. Thus, compared to the other three samples, the Ni/CeO_2-NRs exhibited a higher CH_4 conversion. In the cases of Ni/CeO_2-NRs and Ni/CeO_2-NPs samples, a higher CO_2 conversion was observed compared to CH_4 conversion, which was due to the simultaneous occurrence of reverse water gas shift (RWGS) reaction ($CO_2 + H_2 \rightarrow H_2O + CO$, $\Delta H_{298} = +41$ kJ/mol). However, the CO_2 conversion was lower than CH_4 conversion for Ni/CeO_2-NCs and Ni/CeO_2-NOs samples, which may be caused by the presence of CH_4 thermal decomposition.

The H_2 selectivity increased with increasing the reaction temperature. This was because of the occurrence of carbon gasification, methane decomposition and water-gas shift reaction (WGS) at high temperatures, which can form H_2. The H_2/CO ratios were between 0.45-1.0 over the whole range of temperatures studied and increased with raising the reaction temperature. This ratio values were found to be less than unity, especially at low temperatures. This phenomenon was due to the fact that the RWGS and methanation reaction can consume H_2 at low temperatures.[58]

The TOF of the reaction over Ni/CeO_2 catalysts was calculated by normalizing the observed reaction rate (mol $CH_4/(s \cdot g_{cat})$) to the number of superficial metallic Ni atoms per gram of catalyst (mol Ni/g_{cat}). As the dissociative adsorption of CH_4 was considered to be the rate-determining step, the reaction rate was calculated using the CH_4 conversion. The numbers of exposed nickel atoms per gram of catalyst were calculated assuming $H_{ad}/Ni_{surf} = 1$ by H_2 chemisorption. As displayed in Fig. S1a, the Ni/CeO_2-NRs showed the highest TOF values, followed by the Ni/CeO_2-NOs. With regards to the TOF, the values above 600°C showed the following order: Ni/CeO_2-NRs > Ni/CeO_2-NOs > Ni/CeO_2-NCs > Ni/CeO_2-NPs, whereas at 550 and 600°C, Ni/CeO_2-NCs and Ni/CeO_2-NPs

Table 3 The dispersion and particle size of Ni/CeO_2 catalysts.

Sample	Dispersion [a] (%)	Ni particle size [b] (nm)		
		D1 [c]	D2 [c]	D3 [c]
Ni/CeO_2-NRs	13.2	7.8	6.1	6.4
Ni/CeO_2-NCs	14.3	7.1	5.7	6.5
Ni/CeO_2-NOs	13.7	7.4	5.8	6.2
Ni/CeO_2-NPs	14.4	6.9	5.0	6.3

[a] Dispersion was calculated assuming $H_{ad}/Ni_{surf}=1$.

[b] Metal particle shape was assumed to be spherical.

[c] D1 denoted Ni particle size of the reduced samples determined by chemisorption while D2 and D3 denoted Ni particle size of the reduced samples measured by TEM before and after activity test, respectively.

displayed similar TOFs. From the Arrhenius plots in Fig. S1b based on the methane conversion data, we obtained the related apparent activation energies (E_a). It was evident that crystal-plane had a great influence on the E_a value of the Ni/CeO_2 catalyst. The E_a value of Ni/CeO_2-NRs sample was estimated to be 35.7 kJ/mol, in contrast to the higher values of 41.7 kJ/mol and 40.1 kJ/mol for Ni/CeO_2-NCs and Ni/CeO_2-NOs, respectively. This clearly indicated the considerably higher catalytic activity of the Ni/CeO_2-NRs than that of the other samples.

What is the cause of these differences in the catalytic activity? Above all, the preparation conditions (calcination temperature, time and nickel loading amount, etc.) were the same for all the samples. In addition, according to the previous report, the catalytic activity was sensitive to the number of exposed metallic nickel atoms as well as the size and shape of Ni particles in the reduced catalyst.[59] However, the H_2 chemisorption and TEM results (Fig. 5 and Table 3) showed that the four catalysts had almost the same Ni dispersion (13.2%-14.4%). Moreover, as shown in Fig. 7, the crystallite sizes of Ni active particles anchored on catalysts after activity test remained almost unchanged, and the shape of Ni nanoparticles showed no clear difference among the four catalysts one another. From these results above, it can be concluded that the Ni nanostructure in this study was not the factor leading to the differences in the catalytic activity. Second, this difference can be originated from the nature of the ceria itself. The nanosize effect of ceria should be considered first as it was known to improve the intrinsic reducibility and the formation of oxygen vacancies upon spontaneous reduction of Ce^{4+} to Ce^{3+}. However, the crystallite sizes of as-prepared CeO_2 in our synthesis were between 15-25 nm, which exceeded the reported critical size for the small size effect of CeO_2 (10-15 nm). According to the literature reported by Si et al.,[27] the surface areas of the CeO_2 crystal planes (S_{110}, S_{100}, S_{111}), which were comparable even though they had different widths or diameters, was not the critical factor influencing the activity and selectivity. This encouraged us to speculate that the surface area was not the key parameter affecting the catalytic activity. Based on the above results, a significant parameter to explain this difference of catalytic behavior was the interaction between Ni and CeO_2.

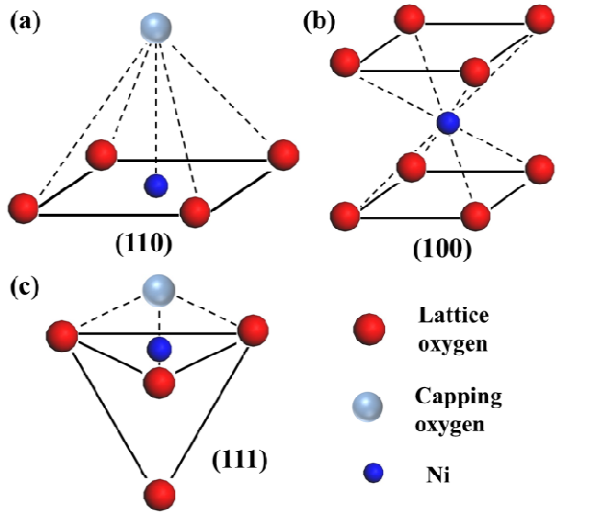

Fig. 8 The tentative models of surface Ni species coordinated with the (110), (100), and (111) planes of CeO_2, respectively.

In this situation, one question to be addressed was that what resulted in the synergistic interaction between Ni and CeO_2. It can be seen that the surface structure, namely, the morphology (crystal plane) of CeO_2, was the key parameter for influencing the interactions between Ni and CeO_2 support. It was well known that CeO_2-NRs, NCs and NOs exposed predominantly the (110), (100), and (111) planes, respectively. The typical structure of CeO_2 can be considered as an array of cations forming the face-centered cubic lattice with oxygen ions locating at the tetrahedral interstitial sites.[23] In a perfect fluorite structure, the octahedral sites were empty and located at the exposed (111) and (110) planes or between (100) planes (Fig. 7). According to the structural characteristics mentioned above, Ni^{2+} can penetrate easily into the lattices of (110) and (111) planes by locating in these sites, accompanied by a capping oxygen for charge compensation. A capping oxygen atom can form unstable five-coordinated structures with four lattice oxygen atoms, such as trigonal bipyramid and square pyramid symmetry (Figs. 8 a and c). In the case of CeO_2-NCs, a part of Ni^{2+} ions can occupy the vacant sites between two (100) planes. One Ni^{2+} ion and eight oxygen atoms formed an eight-coordination structure (Fig. 8b). It was difficult for the rest of Ni^{2+} to move across the oxygen layer as a result of enrichment of Ni species on the surface.[48] The incorporation of Ni^{2+} was considered as an important reason for the generation of interactions between Ni and CeO_2. It was clear that the site geometry and coordination environment of Ni were distinctly different on (110), (100), and (111) planes. This structural effect can result in the differences in the synergistic interaction between Ni and CeO_2, thus influencing the catalytic activity of Ni/CeO_2 catalysts. The above analysis reasonably explained why Ni/CeO_2-NRs and Ni/CeO_2-NOs showed a higher catalytic property than Ni/CeO_2-NCs.

The catalytic stability test of Ni/CeO_2 catalysts was examined at 700 °C for 50 h, and the results were displayed in Fig. 9. A significant decline in CO_2 and CH_4 conversion from 55.6% to 41.8% and from 57.9% to 44.5% were observed over Ni/CeO_2-NCs, respectively. Whereas Ni/CeO_2-NRs exhibited superior stability, with a slight decrease from 77.7% to 75.5% and from 75.4% to 72.8% for CO_2 and CH_4 conversion, respectively. From the XRD and Raman results, it has been proved that CeO_2-NRs showed the largest lattice strain and the relatively highest content of vacancies (Fig. 2 and Fig. 3). Thus, Ni/CeO_2-NRs showed the most stable activity and H_2 selectivity. The Ni/CeO_2-NOs samples underwent slight deactivation during 50 h of TOS. The Ni/CeO_2-NPs exhibited the poorest activity and stability, nearly no activity being observed during stability test after 20 h of TOS. As the conversions of CO_2 and CH_4 were rather low and not sustained, the deactivation of Ni/CeO_2-NPs may be attributed to the

aggregation of Ni particles, which can be evidenced by the XRD and TEM results (Fig. 10 and Fig. 12). This reduced the numbers of Ni active sites and thus affected the catalytic stability. Therefore, the Ni/CeO_2-NRs were superior in methane dry reforming performance under the identical reaction conditions.

The H_2 selectivity and H_2/CO ratio were tracked during the stability test. Ni/CeO_2-NRs catalysts maintained high H_2 selectivity and H_2/CO ratio during 50 h of TOS, while Ni/CeO_2-NOs exhibited moderate H_2 selectivity and H_2/CO ratio. A slight decrease in H_2 selectivity and H_2/CO ratio was also found, which can be due to the further nucleation of Ni particles at the reaction condition after 30 h of TOS. An obvious decrease in H_2 selectivity and H_2/CO ratio was also observed on Ni/CeO_2-NCs. The low H_2/CO ratios over Ni/CeO_2-NPs and Ni/CeO_2-NCs samples revealed the RWGS easily occurred on these two catalysts. This was because of the presence of more unreacted CO_2 under low catalytic activity.

This order was in agreement with that of reducibility (the concentration of oxygen vacancies) of various CeO_2 supports. It was speculated that there was some relation between the lattice strain and the concentration of oxygen vacancies. It was supposed that the asymmetrical five-coordinate structure of Ni/CeO_2-NRs with the largest strain would be unstable, which was favorable for the mobility of surface oxygen. On the contrary, the symmetrical eight-coordination structure of Ni/CeO_2-NCs with the smallest strain would be most stable. Owing to the largest lattice strain and relative highest concentration of oxygen defect, the CeO_2-NRs exhibited the higher catalytic stability and suppression to coking deposition than the other three samples. It was worth noting that the Ni/CeO_2-NPs with (100) and (111) surface should have the higher activity and stability than Ni/CeO_2-NCs for methane dry reforming. However, the Ni/CeO_2-NPs was less active that Ni/CeO_2-NCs. This implied that there were other factors, such as crystalline size, affecting the activity, which would be discussed in the following section.

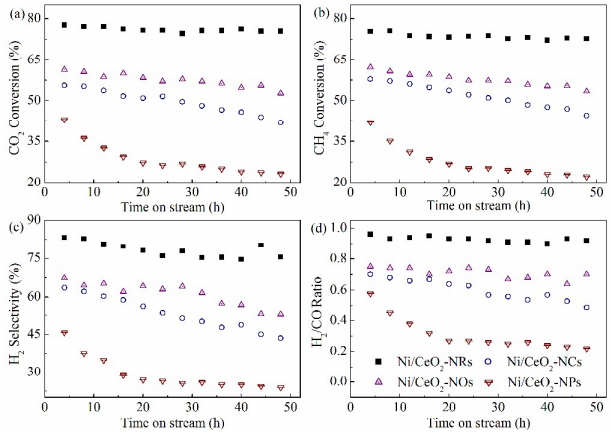

Fig. 9 Catalytic stability test of the Ni/CeO_2 samples for methane dry reforming at 700 °C for 50 h.

Deactivation Analysis

The spent catalysts were characterized by XRD, Raman and TG/DTA to prove the impact of CeO_2 morphology on the carbon deposition. The XRD patterns of spent Ni/CeO_2 catalysts after reaction were presented in Fig. 10a. In the case of spent Ni/CeO_2-NCs sample, a pronounced diffraction peak of graphite phase can be seen at about 26° (Fig. 10b), indicating that large amounts of carbon species with graphitic nature was deposited on the surface of Ni/CeO_2-NCs. However, the graphite peak for the spent Ni/CeO_2-NRs samples was weak, implying its high resistance ability to coke formation. A negligible amount of carbon formation can be also observed on Ni/CeO_2-NPs, which was probably due to its extremely low activity.

The diffraction peaks corresponding to metallic nickel phase can be observed for all of catalysts after reaction, indicating that nickel species were in the metallic state during the reaction. In the cases of Ni/CeO_2-NRs, Ni/CeO_2-NCs and Ni/CeO_2-NOs samples, the diffraction peaks showed a slight difference with those of the reduced counterparts (Fig. 10c). This demonstrated that the Ni particles maintained high dispersion state during the stability test due to the strong metal-support interaction (SMSI). However, the Ni diffraction peak of Ni/CeO_2-NPs became sharper and narrower, indicating the sintering of Ni particles during the stability test.

As the complements of the XRD analysis, the Raman technique can confirm the composition and nature of carbon species on the catalyst surface. As shown in Fig. 10d, both graphite band (G-band) at 1580 cm^{-1} and defect band (D-band) at 1350 cm^{-1} can be observed over all the spent samples, suggesting that both the amorphous carbon and graphite have been formed during the reaction. The obviously higher intensity of G band over the Ni/CeO_2-NCs rather than on the other three samples revealed that the formation of graphite carbon was more likely to occur over the Ni/CeO_2-NCs sample.

The TG/DTA was investigated to quantify the amount of carbon deposit on the catalyst surface. As displayed in Fig. 11, the weight loss of spent catalysts increased with the following

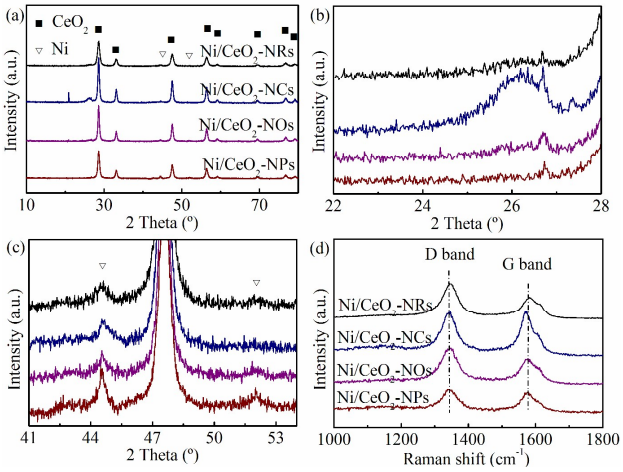

Fig. 10 (a-c) XRD patterns and (d) Raman spectra of spent Ni/CeO_2 samples.

sequence: Ni/CeO_2-NPs (5.5%) < Ni/CeO_2-NOs (18.9%) < Ni/CeO_2-NRs (19.4%) < Ni/CeO_2-NCs (48.9%). The Ni/CeO_2-NCs had the obviously larger weight loss than the other three samples. Negligible amount of carbon was detected on Ni/CeO_2-NPs, which was in line with its poor catalytic activity. From the DTA profiles, two peaks can be observed on the spent samples, indicating that two types of carbon species were deposited on catalyst surface. According to the literatures previously,[6,60,61] the low temperature peak can be ascribed to the oxidation of amorphous carbon, or active carbon species, while the graphitic carbon, namely, inert carbon would be oxidized at high temperatures. When only inert carbon was considered, the amount of deposited carbon increased as the following sequence: Ni/CeO_2-NPs < Ni/CeO_2-NRs < Ni/CeO_2-NOs < Ni/CeO_2-NCs. In the case of Ni/CeO_2-NRs, the large portion of carbon deposition was relative active carbon species, which can participate in the syngas production and was beneficial to prevent the catalyst deactivation to some extent. The disappearance of graphite carbon might be result from the high oxygen vacancies, which can inhibit greatly the carbon deposition on the catalyst surface. The carbon deposited on Ni/CeO_2-NCs was mainly inert species, which can encapsulate the Ni particles at the tail end and was responsible for the catalyst deactivation. In the case of Ni/CeO_2-NPs, the deactivation of Ni/CeO_2-NPs was not due to the carbon deposition but due to the sintering of Ni particles, which was in good agreement with the large particle size (Fig. 10). The tendency to form carbon species over these spent catalysts was consistent with the XRD and Raman results.

In order to further confirm the morphology of the deposited carbon species as well as the Ni particle size, the TEM images of spent samples was performed. As displayed in Fig. 12, all of the Ni/CeO_2 samples basically kept their morphology after reaction. The encapsulating carbon and filamentous carbon species can be easily found over Ni/CeO_2-NCs (Figs. 12d and e), which was in line with the obvious graphite peak evidenced by XRD. The distance between layers of filamentous carbon was 0.337 nm, which was close to that of perfect graphite (0.335 nm), indicating the graphitic structure of the filamentous carbon. In our previous study ,[6,10,60-62] it was found that the filamentous carbon possessed no or little toxicity, while the encapsulating carbon had high toxicity, which can gradually encapsulate the Ni particles, preventing the access of the reacting gases to the active sites. The encapsulating carbon can be clearly seen in Figs. 12d and g. The dark area surrounded by layers of graphitic carbon was one Ni particle with the diameter up to 10 nm. The thickness of these carbon layers were ca. 10 nm. Thus, in the cases of Ni/CeO_2-NCs and Ni/CeO_2-NOs samples, the catalyst surface was covered by graphitic carbon species, resulting in the deactivation. In the cases of Ni/CeO_2-NRs and Ni/CeO_2-NPs, the amount of carbon species was observed to be much lower than the other two samples. However, Ni/CeO_2-NPs sample presented the large Ni particle size up to >20 nm (Fig. 12i), which confirmed that the agglomeration of Ni particles was the factor leading to catalyst deactivation. The Ni particles were located at the tubes tip and have been carried away from the support during the growth process. In the cases of Ni/CeO_2-NRs, Ni/CeO_2-NCs and Ni/CeO_2-NOs samples, the particle size remained unchanged after the stability test due to the SMSI, which was consistent with the XRD results.

Based on the above characterization results, the factors leading to the deactivation can be deduced. Although carbon deposition and metal sintering were the main factors resulting in the activity loss, they played different roles for Ni/CeO_2 catalysts. In case of Ni/CeO_2-NCs, the reason for catalyst deactivation was mainly ascribed to the large amount of carbon deposition in view of the TGA result and the small Ni particle size. In case of Ni/CeO_2-NPs, the deactivation was mainly due to the metal sintering because negligible amount of carbon can be detected.

According to the discussion above, the possible mechanism over the Ni/CeO_2-NRs catalyst was proposed. As shown in Fig. S2, the methane absorbed on the active Ni particles firstly and then decomposed into the active intermediates (CH_x). Ce_2O_3

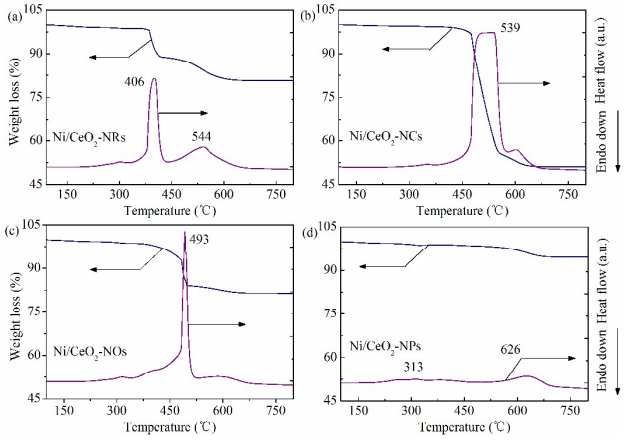

Fig. 11 TG/DTA profiles of spent Ni/CeO_2 catalysts after reaction.

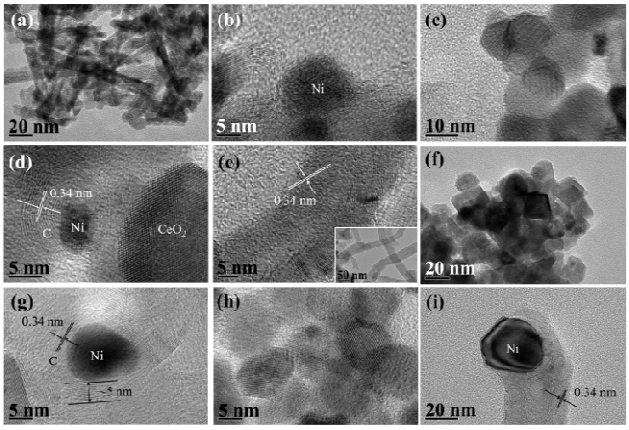

Fig. 12 TEM images of spent samples: (a, b) Ni/CeO_2-NRs, (c-e) Ni/CeO_2-NCs, (f, g) Ni/CeO_2-NOs and (h, i) Ni/CeO_2-NPs.

formed from the reduction of CeO_2 under H_2 atmosphere was re-oxidized by CO_2 during the dry reforming reaction. The obtained CeO_2 can react with CH_x and produced carbon monoxide and hydrogen. The supplement of lattice oxygen came from the dissociation of CO_2 and the oxygen mobility. This process was summarized by following reactions:

$$2CeO_2+H_2 \rightarrow Ce_2O_3+H_2O \quad (6)$$

$$CH_4+Ni \rightarrow Ni\text{-}C+2H_2 \quad (7)$$

$$Ce_2O_3+CO_2 \rightarrow 2CeO_2+CO \quad (8)$$

$$2CeO_2+Ni\text{-}C \rightarrow Ce_2O_3+Ni+CO \quad (9)$$

The oxygen vacancies and oxygen mobility played a significant role on catalytic performance during the methane dry reforming. According to the literature,[63] the C–H bond activation was the kinetically relevant step in the methane dry reforming. The lattice oxygen atoms contributed to the gasification of CH_x, which is helpful to the catalytic activity and the resistance of coke deposition. There were a larger number of oxygen vacancies and higher oxygen mobility on the Ni/CeO_2-NR. Thus, the Ni/CeO_2-NR displayed better coke resistance than the other three catalysts.

Conclusions

We have synthesized four kinds of Ni/CeO_2 catalysts with different morphologies of CeO_2 support (NRs, NCs, NOs, and NPs) and investigated the morphology and crystal-plane effects on catalytic performances in methane dry reforming reaction. The characterization results showed that Ni species can be incorporated into the lattice and induce the increase of oxygen vacancy by occupying the vacant sites. The catalytic properties depended on the shape and exposed plane of CeO_2 supports. Among all the Ni/CeO_2 catalysts, the Ni/CeO_2-NRs exhibited the excellent catalytic behavior in catalytic activity and stability over the other three samples, which was due to the strong anchoring effect of CeO_2-NRs to Ni species. The concentration of oxygen vacancies and the mobility of lattice oxygen in Ni/CeO_2 showed the morphology dependence. They can participate into the catalytic reaction and be favorable for the elimination of carbon deposition. The origin of deactivation for Ni/CeO_2-NCs and Ni/CeO_2-NPs was mainly attributed to the carbon deposition and the sintering of nickel particles, respectively. These results not only revealed that the structure and catalytic behavior of Ni/CeO_2 catalysts can be tuned by controlling the morphology of CeO_2 support but also greatly deepened the understanding of methane dry reforming reaction by Ni/CeO_2 catalysts.

Acknowledgements

The authors thank the support of NSFC program of 21376135, 21506111 and 91434122.

Notes and references

1 K. M. K. Yu, I. Curcic, J. Gabriel and S. C. E. Tsang, *ChemSusChem* 2008, **1**, 893–899.
2 H. W. Kim, A. K. Marcus, J. H. Shin and B. E. Rittmann, *Environ. Sci. Technol.*, 2011, **45**, 5032–5038.
3 P. Markewitz, W. Kuckshinrichs, W. Leitner, J. Linssen, P. Zapp, R. Bongartz, A. Schreiber and T. E. Müller, *Energy Environ. Sci.*, 2012, **5**, 7281–7305.
4 D. Liu, X. Y. Quek, W. N. E. Cheo, R. Lau, A. Borgna and Y. Yang, *J. Catal.*, 2009, **266**, 380–390.
5 L. Xu, H. Song and L. Chou, *ACS Catal.*, 2012, **2**, 1331–1342.
6 N. Wang, K. Shen, L. Huang, X. Yu, W. Qian and W. Chu, *ACS Catal.*, 2013, **3**, 1638–1651.
7 Z. Xu, N. Wang, W. Chu, J. Deng and S. Luo, *Catal. Sci. Technol.*, 2015, **5**, 1588–1597.
8 W. Chu, L. N. Wang, P. A. Chernavskii and A. Y. Khodakov, *Angew. Chem. Int. Ed.*, 2008, **47**, 5052–5055.
9 D. Liu, X.-Y. Quek, H. H. Adeline Wah, G. Zeng, Y. Li and Y. Yang, *Catal. Today*, 2009, **148**, 243–250.
10 N. Wang, K. Shen, X. Yu, W. Qian and W. Chu, *Catal. Sci. Technol.*, 2013, **3**, 2278–2287.
11 C. Dai, S. Zhang, A. Zhang, C. Song, C. Shi and X. Guo, *J. Mater. Chem. A*, 2015, **3**, 16461–16468.
12 S. Zhang, S. Muratsugu, N. Ishiguro and M. Tada, *ACS Catal.*, 2013, **3**, 1855–1864.
13 H. Guo, Y. He, Y. Wang, L. Liu, X. Yang, S. Wang, Z. Huang and Q. Wei, *J. Mater. Chem. A*, 2013, **1**, 7494–7499.
14 S. D. Senanayake, D. Stacchiola, J. Evans, M. Estrella, L. Barrio, M. Pérez, J. Hrbek and J. A. Rodriguez, *J. Catal.*, 2010, **271**, 392–400.
15 N. L. T. Nga, C. Potvin, G. Djéga-Mariadassou, L. Delannoy and C. Louis, *Top. Catal.*, 2007, **42–43**, 91–94.
16 Y. Zhu, S. Zhang, J. Shan, L. Nguyen, S. Zhan, X. Gu and F. Tao, *ACS Catal.*, 2013, **3**, 2627–2639.
17 J. Deng, W. Chu, B. Wang, W. Yang and X. S. Zhao, *Catal. Sci. Technol.*, 2015, doi: 10.1039/c5cy00893j.
18 H. X. Mai, L. D. Sun, Y. W. Zhang, R. Si, W. Feng, H. P. Zhang, H. C. Liu and C. H. Yan, *J. Phys. Chem. B*, 2005, **109**, 24380–24385.
19 Y. Guan, D. A. J. M. Ligthart, Ö. Pirgon-Galin, J. A. Z. Pieterse, R. A. van Santen and E. J. M. Hensen, *Top. Catal.*, 2011, **54**, 424–438.
20 M. Nolan and G. W. Watson, *J. Phys. Chem. B*, 2006, **110**, 16600–16606.
21 X. Liu, K. Zhou, L. Wang, B. Wang and Y. Li, *J. Am. Chem. Soc.*, 2009, **131**, 3140–3141.
22 D. C. Sayle, S. A. Maicaneanu and G. W. Watson, *J. Am. Chem. Soc.*, 2002, **124**, 11429–11439.
23 F. Esch, S. Fabris, L. Zhou, T. Montini, C. Africh, P. Fornasiero, G. Comelli and R. Rosei, *Science*, 2005, **309**, 752–755.
24 V. Shapovalov and H. Metiu, *J. Catal.*, 2007, **245**, 205–214.
25 K. Zhou, X. Wang, X. Sun, Q. Peng and Y. Li, *J. Catal.*, 2005, **229**, 206–212.
26 Q. Dai, H. Huang, Y. Zhu, W. Deng, S. Bai, X. Wang and G. Lu, *Appl. Catal. B*, 2012, **117–118**, 360–368.
27 Z. Wu, M. Li and S. H. Overbury, *J. Catal.*, 2012, **285**, 61–73.
28 W. Chen, K. Chen, M. Wang, S. Weng, C. Lee and M. C. Lin, *Chem. Commun.*, 2010, **46**, 3286–3288.
29 M. Godinho, R. de F. Gonçalves, E. R. Leite, C. W. Raubach, N. L. V. Carreño, L. F. D. Probst, E. Longo and H. V. Fajardo, *J. Mater. Sci.*, 2010, **45**, 593–598.
30 N. Wang, W. Chu, L. Huang and T. Zhang, *J. Nat. Gas Chem.*, 2010, **19**, 117–122.
31 N. Wang, W. Chu, T. Zhang and X. S. Zhao, *Chem. Eng. J.*, 2011, **170**, 457–463.
32 N. Wang, W. Chu, T. Zhang and X. S. Zhao, *Int. J. Hydrogen Energy*, 2012, **37**, 19–30.

33 J. He, T. Xu, Z. Wang, Q. Zhang, W. Deng and Y. Wang, *Angew. Chem. Int. Ed.*, 2012, **51**, 2438–2442.
34 X. S. Huang, H. Sun, L. C. Wang, Y. M. Liu, K. N. Fan and Y. Cao, *Appl. Catal. B*, 2009, **90**, 224–232.
35 J. Li, N. Ta, Y. Li and W. J. Shen, *Chin. J. Catal.*, 2008, **29**, 823–830.
36 S. Yang and L. Gao, *J. Am. Chem. Soc.*, 2006, **128**, 9330–9331.
37 C. Pan, D. Zhang, L. Shi and J. Fang, *Eur. J. Inorg. Chem.*, 2008, **15**, 2429–2436.
38 J. Zhang, H. Kumagai, K. Yamamura, S. Ohara, S. Takami, A. Morikawa, H. Shinjoh, K. Kaneko, T. Adschiri and A. Suda, *Nano Lett.*, 2011, **11**, 361–364.
39 A. Martínez-Arias, A. B. Hungría, M. Fernández-García, J. C. Hanson and G. Munuera, *J. Phys. Chem. B*, 2004, **108**, 17983–17991.
40 J. A. Rodriguez, X. Wang, G. Liu, J. C. Hanson, J. Hrbek, C. H. F. Peden, A. Iglesias-Juez and M. Fernández-Garc, *J. Mol. Catal. A*, 2005, **228**, 11–19.
41 J. Guzman, S. Carrettin and A. Corma, *J. Am. Chem. Soc.*, 2005, **127**, 3286–3287.
42 L. Ilieva, G. Pantaleo, I. Ivanov, A. M. Venezia and D. Andreeva, *Appl. Catal. B*, 2006, **65**, 101–109.
43 J. Lin, L. Li, Y. Huang, W. Zhang, X. Wang, A. Wang and T. Zhang, *J. Phys. Chem. C*, 2011, **115**, 16509–16517.
44 T. Taniguchi, T. Watanabe, N. Sugiyama, A. K. Subramani, H. Wagata, N. Matsushita and M. Yoshimura, *J. Phys. Chem. C*, 2009, **113**, 19789–19793.
45 Z. Wu, M. Li, J. Howe, H. M. Meyer III and S. H. Overbury, *Langmuir*, 2010, **26**, 16595–16606.
46 X. Q. Wang, J. A. Rodriguez, J. C. Hanson, D. Gamarra, A. Martínez-Arias and M. Fernández-García, *J. Phys. Chem. B*, 2005, **109**, 19595–19603.
47 A. E. Nelson and K. H. Schulz, *Appl. Surf. Sci.*, 2003, **210**, 206–221.
48 L. J. Liu, Z. J. Yao, Y. Deng, F. Gao, B. Liu and L. Dong, *ChemCatChem*, 2011, **3**, 978–989.
49 M. S. P. Francisco, V. R. Mastelaro, P. A. P. Nascente and A. O. Florentino, *J. Phys. Chem. B*, 2001, **105**, 10515–10522.
50 C. T. Campbell and C. H. F. Peden, *Science*, 2005, **309**, 713–714.
51 M. Boaro, F. Giordano, S. Recchia, V. Dal Santo, M. Giona and A. Trovarelli, *Appl. Catal. B*, 2004, **52**, 225–237.
52 A. E. C. Palmqvist, M. Wirde, U. Gelius and M. Muhammed, *Nanostruct. Mater.*, 1999, **11**, 995–1007.
53 C. M. Chanquía, K. Sapag, E. Rodríguez-Castellón, E. R. Herrero and G. A. Eimer, *J. Phys. Chem. C*, 2010, **114**, 1481–1490.
54 L. Huang, J. Xie, R. Chen, D. Chu and A. T. Hsu, *Mater. Res. Bull.*, 2010, **45**, 92–96.
55 L. Huang, Q. Liu, R. Chen and A. T. Hsu, *Appl. Catal. A*, 2011, **393**, 302–308.
56 W. Shan, M. Luo, P. Ying, W. Shen and C. Li, *Appl. Catal., A*, 2003, **246**, 1–9.
57 A. Caballero, J. P. Holgado, V. M. Gonzalez-delaCruz, S. E. Habas, T. Herranz and M. Salmeron, *Chem. Commun.*, 2010, **46**, 1097–1099.
58 X. Y. Quek, D. Liu, W. N. E. Cheo, H. Wang, Y. Chen and Y. Yang, *Appl. Catal. B*, 2010, **95**, 374–382.
59 Y. H. Wang, H. M. Liu and B. Q. Xu, *J. Mol. Catal. A*, 2009, **299**, 44–52.
60 N. Wang, X. Yu, K. Shen, W. Chu and W. Qian, *Int. J. Hydrogen Energy*, 2013, **38**, 9718–9731.
61 N. Wang, X. Yu, Y. Wang, W. Chu and M. Liu, *Catal. Today*, 2013, **212**, 98–107.
62 N. Wang, Z. Xu, J. Deng, K. Shen, X. Yu, W. Qian, W. Chu and F. Wei, *ChemCatChem*, 2014, **6**, 1470–1480.
63 J. Wei and E. Iglesia, *J. Catal.,* 2004, **224**, 370–383.

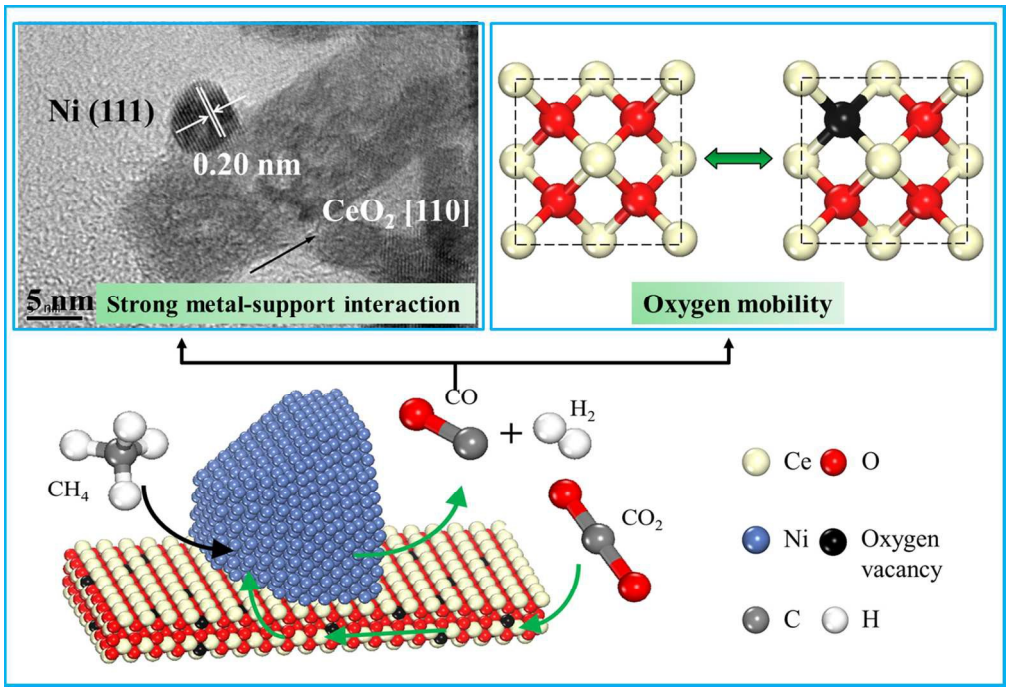

238x162mm (150 x 150 DPI)